

Three-dimensional simulation of an inductively coupled plasma reactor

Theodoros Panagopoulos,^{a)} Doosik Kim, Vikas Midha,^{b)} and Demetre J. Economou^{c)}

Plasma Processing Laboratory, Department of Chemical Engineering, University of Houston, Houston, Texas 77204-4004

(Received 2 August 2001; accepted for publication 11 December 2001)

A three-dimensional finite element fluid model and a corresponding simulation tool have been developed for studying azimuthal asymmetries and their effect on etch uniformity in inductively coupled plasma (ICP) reactors. For silicon etching with chlorine in an ICP reactor with a planar coil, four different cases were examined: (a) uniform power deposition without a focus ring, (b) uniform power deposition with a focus ring, (c) nonuniform power deposition without a focus ring, and (d) nonuniform power deposition with a focus ring. When etching is ion driven, the power deposition profile is most important for etch uniformity, because azimuthal nonuniformities in the ion production rate can persist even down to the wafer level. For uniform power deposition, the effect of asymmetric pumping becomes more important. A focus ring can play an important role in alleviating azimuthal nonuniformities, especially in the nonuniform power deposition cases. Gas inlets pointing parallel to the wafer plane introduce only local disturbances in the species profiles.

© 2002 American Institute of Physics. [DOI: 10.1063/1.1448673]

I. INTRODUCTION

Inductively coupled plasma (ICP) reactors operating at low gas pressure (<50 mTorr) to improve uniformity and high plasma density ($>10^{11}$ cm $^{-3}$) to deliver a high flux of ions and radicals to the wafer surface are widely employed for microelectronic device fabrication.¹ Several two-dimensional (2D) models²⁻⁶ have been developed to simulate ICP reactors. In all these models azimuthally symmetric profiles for power deposition and chemical species densities were assumed. Although 2D models are useful for understanding plasma transport and for studying etch rate variations along the wafer radius, they are not able to address issues related to azimuthal asymmetries inherent in many practical ICP systems. Three-dimensional simulations⁷⁻⁹ are computationally more expensive but they can capture any azimuthal asymmetries introduced by gas inlets, pumping ports, and nonuniform power deposition profiles. This becomes more important as wafer sizes increase to 300 mm and beyond in diameter.⁹

In this work, a three-dimensional (3D) finite element fluid model was developed to examine the effect of gas inlets, the pumping port, and nonuniform power deposition profiles on the species densities and etch uniformity in ICP reactors. For this, a two-dimensional ICP simulation tool,^{10,11} a modular plasma reactor simulator (MPRES), was extended to three dimensions to include the azimuthal coordinate. The resulting simulation tool, the MPRES-3D, was used to analyze silicon etching with chlorine in an ICP with a stovetop (planar) coil. Four different cases were examined: (a) azimuthally uniform power deposition (henceforth called uniform power deposition) without a focus ring, (b) azimuthally

uniform power deposition with a focus ring, (c) nonuniform power deposition without a focus ring, and (d) nonuniform power deposition with a focus ring. Actually, for the uniform power deposition cases [(a) and (b)], it was the coil *current* that was kept azimuthally uniform. In this case, there could still be slight azimuthal nonuniformities of the power deposition due to azimuthal nonuniformities of the electron density. To our knowledge, the effect of a focus ring on species profiles and etch uniformity has not been studied computationally so far.

II. MODEL FORMULATION

MPRES-3D is a finite element package that can be used to perform self-consistent simulations of plasma transport in arbitrary three-dimensional ICP reactors using arbitrary gas phase and surface chemistries. The finite element mesh is constructed using FEMAP (a commercial package from a division of Structural Dynamics Research Corporation, Milford, OH), a general-purpose grid generator. MPRES-3D consists of five modules (Fig. 1). The simulation begins with the “electromagnetics module” by solving Maxwell’s equations to determine the electromagnetic fields and plasma power deposition profiles for a specified total power. This is achieved with a procedure similar to that developed by Jaeger and co-workers,¹² as outlined in Midha and Economou.¹³ The power deposition profile is used as input to an “electron energy module” to calculate the electron “temperature” and therefrom the rate coefficients of electron-impact reactions. In turn, these are used in the “source” terms of the “charged species reaction and transport module” and the “neutral species reaction and transport module.” The former is used to calculate the charged species densities, while the latter is used to calculate the neutral gas composition. The calculation is repeated in a cyclical fashion until “convergence.” From the converged solution, the self-consistent power deposition, electrostatic potential, electron temperature, charged

^{a)}Present address: Applied Materials Inc., Santa Clara, CA 95054.

^{b)}Present address: General Electric-CRD, Schenectady, NY 12065.

^{c)}Author to whom correspondence should be addressed; electronic mail: economou@uh.edu

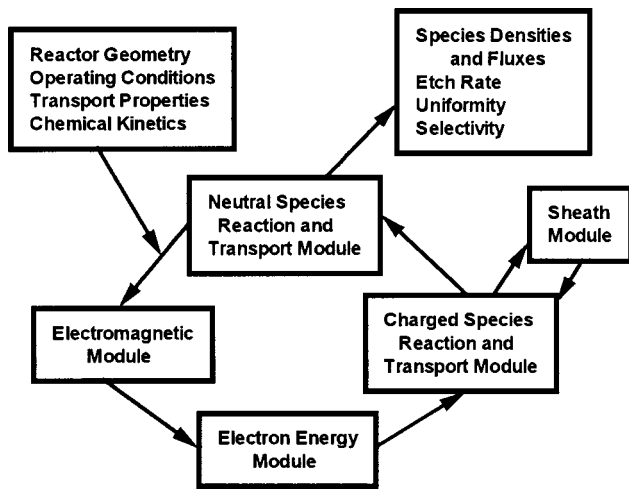


FIG. 1. Modular approach followed in MPRES-3D. The simulation requires as input the reactor geometry and materials of construction, operating conditions, transport properties of the species of interest, and chemical kinetics. The simulation starts with the “electromagnetics module” and cycles through the modules until convergence. An optional “sheath module” can be activated to calculate time-dependent potentials and ion energy distributions. The simulation outputs the species densities and fluxes, etch rate, uniformity, and selectivity across the wafer.

and neutral species densities, and flux, etch (or deposition) rate and uniformity, as well as selectivity over the wafer surface can be calculated. A “sheath module” can be used as a postprocessing step to calculate the time-dependent plasma, substrate and wall potentials, the dc bias developed on the wafer electrode, and the energy distribution function of ions bombarding the wafer. The sheath is described by a semianalytical model.^{14,15} Two-dimensional MPRES simulation results for argon, chlorine, and mixed chlorine/boron trichloride chemistries, and comparisons with experimental data can be found in Refs. 10, 11, and 16.

A. Approximations made in MPRES-3D

A number of simplifying approximations, based on the physics of the problem, are made in MPRES-3D to speed up the calculation.

1. Separation of bulk plasma from the sheath

For high density plasmas (HDPs), the sheath thickness is on the order of hundreds of μm . In contrast, the reactor dimension is typically tens of cm. This disparity in length scales requires, for any numerical method, a much denser grid near the walls compared to the bulk plasma. The high degree of spatial stiffness (10^3) introduces numerical difficulties and results in excessive computation times. For this reason it has become customary to separate the bulk plasma from the sheath, or to avoid resolving the sheath. Fortunately, the sheath in HDPs is collisionless, since the species mean free path at 10 mTorr is on the order of 1 cm, much larger than the sheath thickness. Thus, if one knows the ion (or electron) distribution function at the sheath edge and the spatiotemporal distribution of the sheath electric field, one can obtain the ion (or electron) distribution function at the wall. In order to be consistent with the Bohm criterion for ions, the sheath edge is defined as the point where the ions have been

accelerated (by the presheath electric field) to the Bohm velocity, i.e., the presheath is included as part of the bulk plasma. The Bohm flux also provides a boundary condition (applied at the wall because of the thinness of the sheath) for the positive ion continuity equation. The negative ion density is assumed to be zero at the boundary.

2. Electroneutrality in the bulk plasma

If one is not interested in resolving length scales of the order of the Debye length, the electroneutrality constraint in the bulk plasma is applicable

$$n_e = \sum_i z_i n_i, \quad (1)$$

where n_i is the number density of ion i and z_i is the number of elementary charges on the ion; it is positive for positive ions and negative for negative ions. Equation (1) is an excellent approximation for the plasmas of interest since the Debye length is exceedingly small (tens of μm) compared to the reactor’s dimensions. Of course, the electroneutrality constraint cannot be applied in the sheath, where the Poisson equation has to be solved. Solving Poisson’s equation in the whole reactor domain introduces numerical difficulties. When using the electroneutrality constraint, the electron continuity equation is not necessary. The electron density is obtained directly from Eq. (1), having solved for all ion densities.

3. Boltzmann electrons

If the Poisson equation is used instead of electroneutrality in the bulk, the electrostatic field can be recovered without the need for recourse to any additional assumptions. Since the Poisson equation is not solved in the bulk, the space charge fields are obtained by assuming Boltzmann electrons,

$$\mathbf{E}_{sc} = - \frac{\nabla(n_e k T_e)}{en_e}, \quad (2)$$

where T_e is the space-dependent electron temperature, k is the Boltzmann constant, and e is the elementary charge. This expression results from the electron momentum balance by assuming inertialess electrons (neglecting the left-hand side of the momentum equation).¹ The electron drift and diffusion fluxes nearly balance each other, yielding Eq. (2). This equation simply states that the electric field force balances the electron pressure force. Equation (2) breaks down when the density of negative ions is large enough such that the negative ion current is an appreciable fraction of the current carried by negatively charged species. In such a case the more general expression for the field resulting from the ambipolar constraint may be used,

$$\mathbf{E}_{sc} = \left(\frac{\sum_i z_i D_i \nabla n_i - D_e \nabla n_e}{\sum_i \mu_i n_i + \mu_e n_e} \right), \quad (3)$$

where D and μ are the diffusivity and mobility of the respective charged species. Under typical ICP conditions in this work, however, the negative ion density is comparable to the electron density and Eq. (2) is applicable.

4. Specified electron energy distribution function

The electron energy distribution function (EEDF) is assumed to be Maxwellian, a commonly employed approximation based on the fact that the high electron density of HDPs helps in “Maxwellianizing” the EEDF. A bi-Maxwellian distribution may be more appropriate for lower electron densities. The shape of the distribution is not expected to have a great effect on the ion densities since the ionization rate is self-adjusted to balance the rate of loss of ions to the walls, and the latter depends only very weakly on the EEDF. A bi-Maxwellian or other forms of the EEDF may also be used in MPRES-3D. Of course, if accurate determination of the EEDF is necessary, one must solve the Boltzmann equation.

5. Drift diffusion for ions

The drift–diffusion approximation is made for ions, e.g., ion inertia is neglected. This appears to be a good approximation for $Kn < 0.2$ (~ 10 mTorr for typical ICPs). Equation (2) (or Eq. 3) provides the field that drives ions in the plasma.

6. Diffusive flow for neutrals

The importance of convective versus diffusive flow of neutrals is determined by the Peclet number, $Pe = uL/D$, where u is the gas convective velocity, L is a characteristic dimension of the system, and D is the diffusivity of the species. Away from inlet and exit ports, the characteristic length will be on the order of the reactor dimensions. The system will be primarily diffusive when $Pe \ll 1$. For Cl_2 gas in a reactor with $L \sim 0.1$ m and a neutral species diffusivity of $D \sim 5 \text{ m}^2 \text{ s}^{-1}$ at 20 mTorr, the Peclet number will be $Pe \sim 1$ when $u = 50 \text{ m s}^{-1}$. Convective gas velocities are not likely to be that high, except for in a small region near the gas inlet ports. It follows that gas flow can be approximated as diffusive; this obviates the need for solving the full Navier–Stokes equations which adds to the computational burden. It should be noted that both the diffusivity and the convective velocity scale inversely with gas pressure, so the Pe number is independent of the pressure. However, as the pressure is lowered to the point of free molecular flow, the gas diffusion coefficient no longer has any meaning. Direct simulation Monte Carlo (DSMC) may then be applied to solve the fluid velocity profiles.

7. Ohmic power deposition

In ohmic power deposition it is assumed that the electron mean free path is smaller than the skin depth of inductive power deposition and that the electron collision frequency is larger than the frequency of the applied field.¹⁷ These approximations are thought to be valid for the pressure of 10 mTorr examined in this work.

Based on the above approximations, the following mathematical formulation of the problem results.

B. Electromagnetics module

The electromagnetics module is based on the work of Jaeger *et al.*¹² as implemented by Midha and Economou.¹³ Combining Faraday’s and Ampere’s laws, one can obtain the vector wave equation,

$$\nabla^2 \mathbf{E} + \frac{\omega^2}{c^2} K_c \mathbf{E} = -j\omega\mu_0 \mathbf{J}, \quad (4)$$

where \mathbf{E} is the electric field that powers the plasma, ω is the radian frequency of the applied current, c is the speed of light, K_c is the (complex) relative permittivity of the medium, μ_0 is the magnetic permeability of free space, and \mathbf{J} is the impressed current which follows the contour of the induction coil. The planar coil is represented by a set of discrete concentric loops. Thus, the impressed current J_θ and the resulting electric field E_θ have only an azimuthal component along the θ direction.

The following strategy was used to compute the 3D power deposition profiles. A 2D (r, z) electromagnetics (EM) simulation was performed first, as outlined in Ref. 13, to calculate the variation of current from coil to coil due to capacitive coupling (discussed below). In this 2D EM simulation, the current within each coil was assumed to be azimuthally invariant. A linear variation of the current was then assumed along each coil with the continuity of current required at the end of a coil and the beginning of the next coil. This is valid provided that the coil length is shorter than a quarter wavelength. Based on the azimuthally varying current, Eq. (4) was solved in three dimensions to calculate the power deposition profile.

For the 2D calculation, azimuthally averaged values of the plasma density and electron temperature were used to compute the relative permittivity of the plasma K_c in Eq. (4),

$$\langle n_e \rangle = \frac{1}{2\pi} \int_0^{2\pi} n_e d\theta,$$

and (5)

$$\langle T_e \rangle = \frac{1}{2\pi} \int_0^{2\pi} T_e d\theta.$$

At relatively high frequencies (more than about 5 MHz in our case) capacitive coupling may be significant and a circuit model is required to compute the variation of current from coil to coil. The capacitive current in loop “ i ” of the coil is defined as the rate of change of charge accumulated in the volume of the coil,

$$I_c^i = \frac{d}{dt} \int_{V_i} \rho dV = -i\omega\epsilon_0 \int_{V_i} \nabla \cdot (K_c \mathbf{E}) dV, \quad (6)$$

where ϵ_0 is the permittivity of free space. The change in current from one loop of the coil to the next may be found by computing the average value of the capacitive current I_c in the two loops,

$$I_i^i - I_i^{i+1} = \langle I_c \rangle = \frac{1}{2}(I_c^i + I_c^{i+1}). \quad (7)$$

Each loop of the coil is modeled as a lumped electrical network. The inductive voltage drop across the i th loop V_l is given by

$$V_l^i = V_{in}^i - V_{out}^i = - \int_{l_i} E_{\theta} dl, \quad (8)$$

where l_i is the length of the i th loop. The overall equivalent circuit is completed by connecting all N networks in series (for N loops of the coil). The first loop is driven by a specified current, I_{sp} , and the N th loop is connected to ground through a specified impedance, Z_{sp} . The continuity of the voltages and currents for the N loops may be expressed as

$$V_{in}^i = V_{out}^{i-1}, \quad (9)$$

$$V_l^i = V_{in}^i - V_{out}^i, \quad (10)$$

$$I_{in}^i = I_{out}^{i-1}, \quad (11)$$

$$I_c^i = I_{in}^i - I_{out}^i, \quad (12)$$

where for $i=1$, $I_{in}^1 = I_{sp}$ and for $i=N$, $V_{out}^N = I_{out}^N Z_{sp}$.

The values of I_l^i and V_l^i depend on details of the network used to approximate each loop. Some of the possible choices include a transmission line or the “ T ” equivalent of a transmission line (the former choice was made in this work). For either network, Eqs. (9)–(12) can be solved iteratively to calculate the (constant) current in each loop. As mentioned before, the current was then assumed to vary linearly along each loop and Eq. (4) was solved in 3D.

Once the electric field distribution is known, the time-averaged value of the power density deposited in the plasma due to ohmic heating may be evaluated by

$$P = \frac{1}{2} \sigma_p |\mathbf{E}|^2, \quad (13)$$

where P is the power density, σ_p is the complex plasma conductivity,

$$\sigma_p = \frac{n_e e^2}{m_e (\nu_e + j\omega)}, \quad (14)$$

and $|\mathbf{E}|^2$ is the square of the modulus of the electric field. In Eq. (14), n_e is the electron density, e is the elementary electric charge, m_e is the electron mass, and ν_e is an effective momentum–transfer collision frequency. The last may be used instead of the actual electron momentum collision frequency ν_m to account for nonlocal power deposition at low pressures.¹⁸ In this work it was assumed that $\nu_e = \nu_m$, which appears to be a good approximation.

1. Electron energy module

The electron energy balance is described by

$$\frac{\partial}{\partial t} \left(\frac{3}{2} n_e k T_e \right) + \nabla \cdot \mathbf{q}_e + 3 \frac{m_e}{M} n_e k \nu_m (T_e - T_g) - P + \sum_j H_j R_j = 0, \quad (15)$$

where \mathbf{q}_e is the total electron energy flux [composed of a conduction and a convection term; see Eq. (16)], T_g is the gas temperature, and P is the power deposited into the

plasma [Eq. (13)]. The third term on the right-hand side of Eq. (15) represents energy loss in elastic collisions and the last term accounts for energy loss due to inelastic electron collisions. The total electron energy flux is given by

$$\mathbf{q}_e = -K_e \nabla T_e + \frac{5}{2} k T_e \mathbf{J}_e, \quad (16)$$

where the thermal conductivity of electrons is $K_e = \frac{3}{2} k D_e n_e$, and D_e is the electron diffusivity.

2. Charged species reaction and transport module

The densities of the charged particles are computed by solving the mass continuity equation,

$$\frac{\partial n_i}{\partial t} + \nabla \cdot \mathbf{J}_i = \sum_j R_j, \quad (17)$$

where n_i and \mathbf{J}_i are the density and flux, respectively, of charged species i . The summation in Eq. (17) is over all reactions that consume or produce species i . Charged species included in the calculation were Cl^+ , Cl_2^+ and Cl^- .

Instead of solving the momentum equation, the drift–diffusion approximation was adopted for describing the motion of charged particles. Assuming slow time variation and neglecting both the inertial and magnetic forces for ions, the flux was approximated by

$$\mathbf{J}_i = -D_i \nabla n_i + z_i \mu_i n_i \mathbf{E}_{sc}. \quad (18)$$

The Poisson equation was not solved in the bulk of the plasma. The quasineutrality condition [Eq. (1)] was used instead. As a result, a mass balance equation for electrons was not necessary since their density is obtained directly from Eq. (1).

3. Neutral species reaction and transport module

The mass balance for neutral species is

$$\frac{\partial n_*}{\partial t} + \nabla \cdot (-D_* \nabla n_*) = \sum_j R_j, \quad (19)$$

where n_* and D_* represent the density and the diffusion coefficient of neutrals, respectively. Equation (19) implies that the flux of neutrals is dominated by diffusion. The summation is over all source/sink reactions that involve the species under consideration, including electron impact as well as neutral–neutral and neutral–ion reactions. The neutral species included are Cl , Cl_2 , and the reaction product SiCl_2 . The chemistry set was the same as before,² assuming an “average” reaction product SiCl_2 . We recognize that for high neutral to ion flux ratios, more chlorinate products may result (up to SiCl_4). Use of an average SiCl_2 product presumes rapid plasma dissociation of the more chlorinated compounds. The transport data (mobilities, diffusivities) were also identical to those in Ref. 2.

4. Boundary conditions

The electron energy at the wall was taken as

$$\mathbf{q}_e = \frac{5}{2} k T_e \mathbf{J}_e, \quad (20)$$

where the electron particle flux was computed through the ambipolar approximation,

$$\mathbf{J}_e = \sum_{i \neq e} z_i \mathbf{J}_i \quad (21)$$

The flux of positive ions was equal to the Bohm flux at the sheath–presheath boundary, neglecting the concentration of negative ions there,

$$J_+ = n_s u_{B_i} = n_s \sqrt{\frac{kT_e}{m_i}} \quad (22)$$

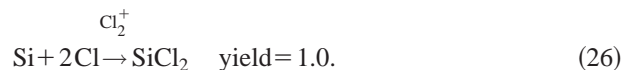
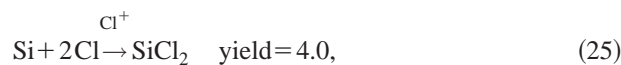
where n_s is the ion density at the sheath–presheath boundary. The negative ion density was taken to be zero at the boundary since negative ions are repelled by the sheath. A modified thermal flux of neutrals, given by Chantry,¹⁹ is

$$J_* = \frac{2\gamma}{2-\gamma} \frac{1}{4} \sqrt{\frac{8kT_g}{\pi m}} n_* \quad (23)$$

where γ is the recombination probability of the neutral species, taken here as 0.1 for Cl and 0 for the rest. The net flux of Cl atoms was set equal to the modified thermal flux minus the neutralization flux of atomic chlorine ions. At the pumping port the flux of neutrals is given by

$$J_* = K_p n_* \quad (24)$$

where K_p is a pumping speed (m/s). The flux of Cl₂ at the inlet ports was set by the specified inlet flow rate. For calculation of the Si wafer etch rate the following surface reactions were assumed:



The reactions are ion induced with the Cl⁺ ion yield being four times higher²⁰ than that of Cl₂⁺.

The method of lines was used for numerical solution of the governing equations. The equations were discretized by a finite element method using tetrahedral elements. The grid was generated by FEMAP. The resulting set of ordinary differential equations was integrated in time with a stiff integrator (LSODI) using backward difference formulas.^{2,11}

III. RESULTS AND DISCUSSION

Nonuniformities, especially those in the azimuthal direction which are caused by gas inlets, pumping ports, and nonuniform power deposition in a cylindrical reactor, were studied for chlorine discharge plasmas. Figure 2(a) shows a schematic of the reactor that has a height of 15 cm and a diameter of 40 cm. Four gas inlets, pointed horizontally, are located symmetrically around the periphery of the reactor, on a plane 12.4 cm from the wafer level. A pumping port (2.6 cm high measured from the wafer level and 31.4 cm in arc length) is located at the lower left quadrant of the chamber. Figure 2(b) gives a view of the reactor floor as seen from the top. A 300 mm wafer, flush with the reactor floor, is denoted by the center hatched area. A cylindrical focus ring (outlined by the dashed lines surrounding the wafer) has a height of 2.6 cm measured from the wafer level. The planar antenna coil is represented as three annuli located on the top of the

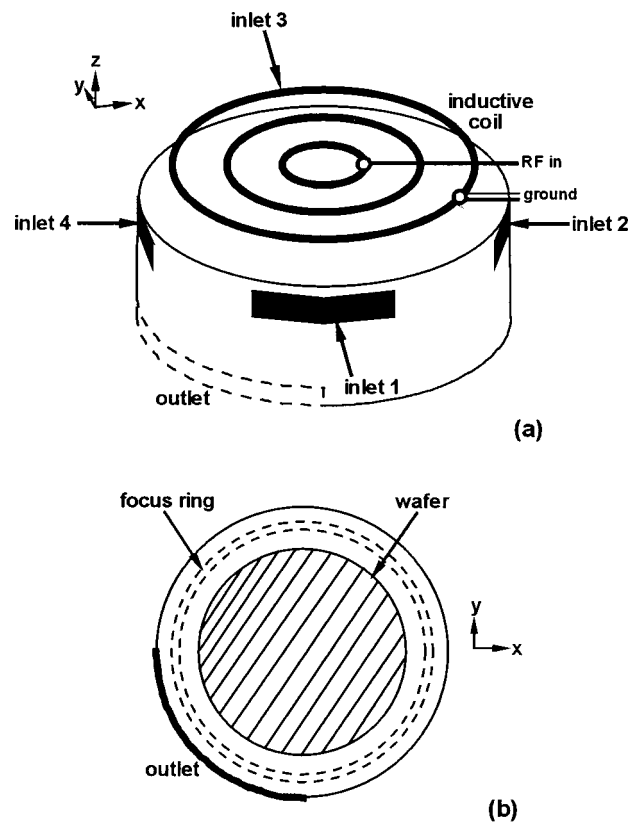


FIG. 2. Schematic diagram of the cylindrical reactor (400 mm inside diameter, 150 mm inside height) used in this study: (a) 3D view showing the location of the outlet port (in the lower left quadrant). The inductive coil is represented by three concentric current loops; the power tap and grounded end are also shown (b) Top view of the reactor floor showing the 300 mm diam wafer zone and the location of the focus ring that surrounds the wafer.

reactor as shown in Fig. 2(a). A quartz window (not shown) separates the coil from the plasma. The coil current is at a minimum at the input and maximum at the ground due to capacitive coupling. The termination impedance was assumed to be zero.

The following were the base conditions: nominal pressure 10 mTorr, 13.56 MHz rf power deposition of 2000 W, gas temperature 500 K, and feed flow rate 79 sccm of pure Cl₂ gas. In order to streamline the investigation of azimuthal asymmetries, four different configurations, all at the base conditions, were studied: (a) uniform power deposition without a focus ring, (b) uniform power deposition with a focus ring, (c) nonuniform power deposition without a focus ring, and (d) nonuniform power deposition with a focus ring. For the uniform power deposition cases the coil current was assumed to be constant within each loop, but the current increased (due to capacitive coupling) from the inner to the outer loop of the coil. Thus, the current varied in the radial direction only. For the nonuniform power deposition cases, the current was assumed to increase linearly along the path of the coil. Thus, in this case, the current varied in both radial and azimuthal directions.

Figure 3 shows power deposition profiles at a horizontal cross section 1 cm below the bottom of the quartz window. Most of the electromagnetic power is deposited within the skin's depth (~1 cm). In the uniform power deposition cases

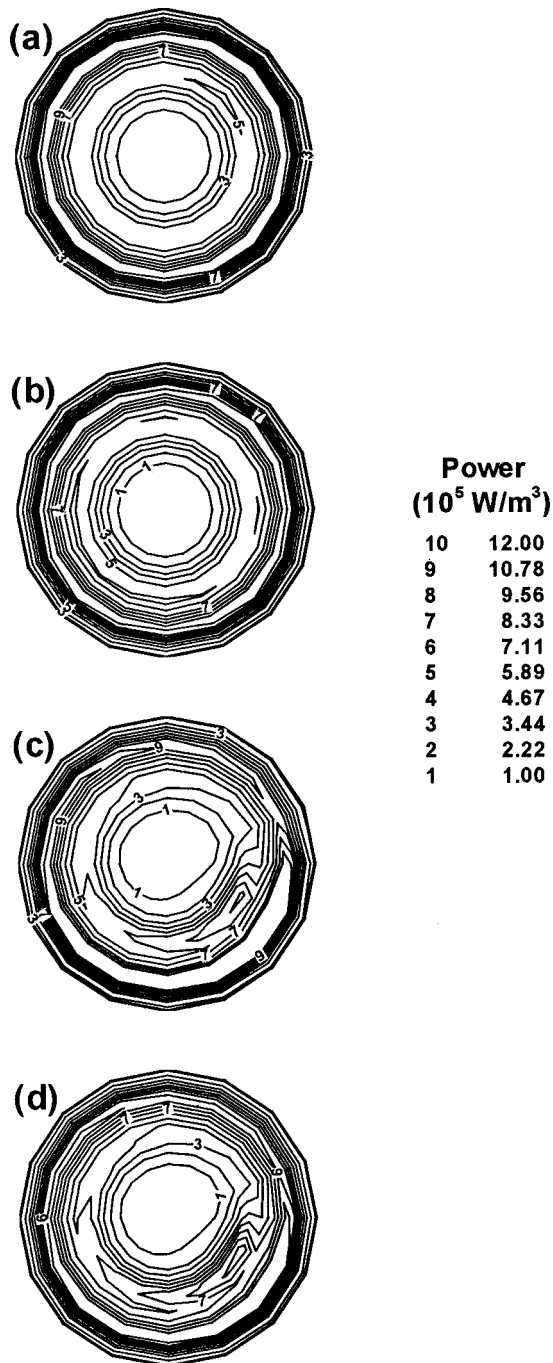


FIG. 3. Inductive power deposition (W/m^3) profiles at a horizontal plane 14 cm from the wafer plane: (a) uniform power deposition without a focus ring, (b) uniform power deposition with a focus ring, (c) nonuniform power deposition without a focus ring, and (d) nonuniform power deposition with a focus ring.

[(a) and (b)], power deposition is highest near the outer coil where the current is highest. Slight azimuthal nonuniformities of the power deposition in cases (a) and (b) are due to azimuthal disturbance of the electron density profile due to the presence of the inlet and pumping ports. [Note that the *current* was assumed azimuthally uniform in cases (a) and (b), not the power deposition.] For the nonuniform power deposition cases, power absorption peaks at the azimuthal position near the ground end of the coil, where the current is highest. The focus ring makes the power deposition profile

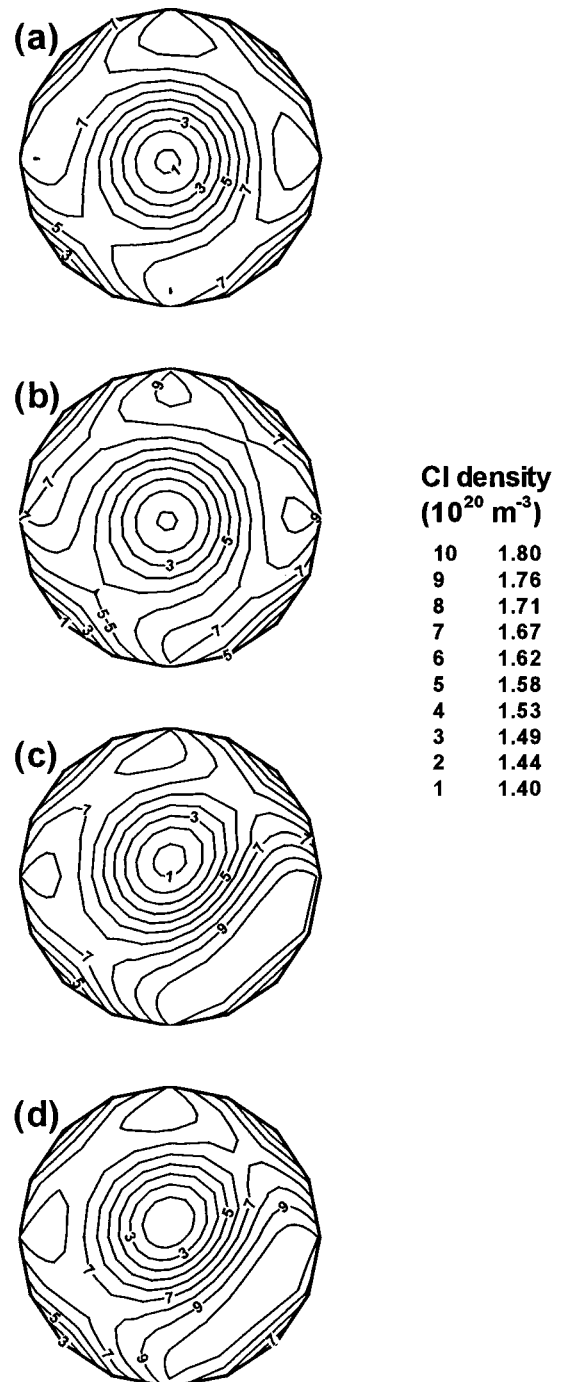


FIG. 4. CI density (m^{-3}) profiles at a horizontal plane 14 cm from the wafer plane: (a) uniform power deposition without a focus ring, (b) uniform power deposition with a focus ring, (c) nonuniform power deposition without a focus ring, and (d) nonuniform power deposition with a focus ring.

slightly more symmetric in the azimuthal direction [compare cases (c) and (d)], mainly because the electron density is slightly more symmetric in case (d).

For high enough pressures, the electron impact reaction rates mirror the power deposition profiles. The CI density profile 1 cm below the quartz window is shown in Fig. 4. The CI density is at a minimum at the center and increases towards the periphery, only to drop again near the cylindrical wall. CI atoms are created mainly where power is deposited and diffuse to fill in the center zone of the reactor. At axial

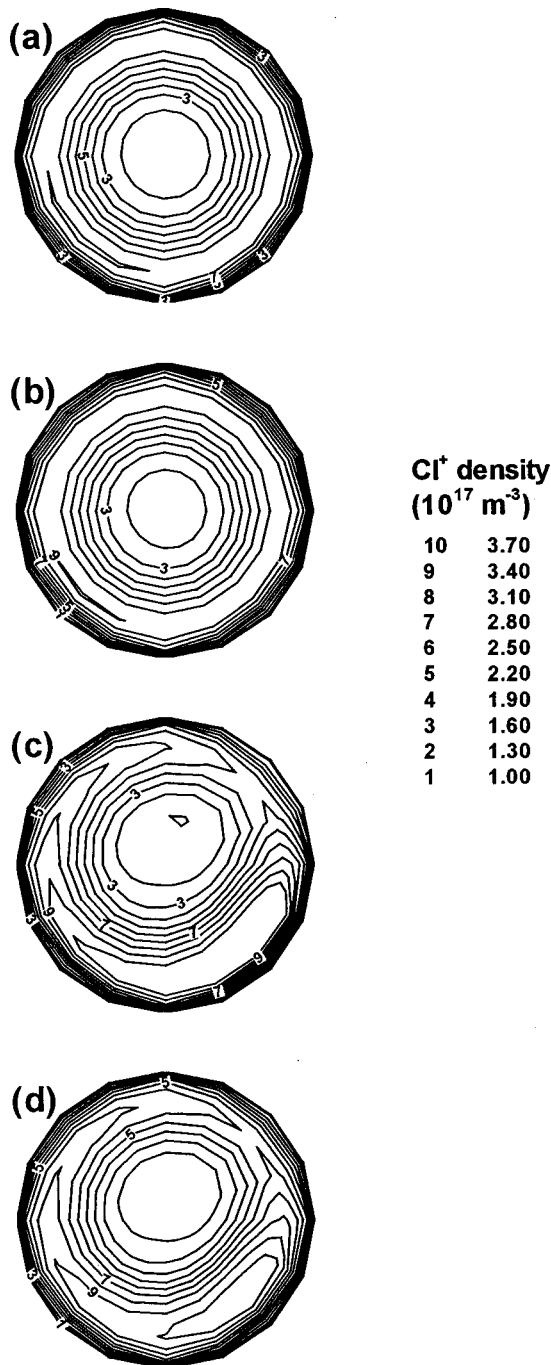


FIG. 5. Cl^+ density (m^{-3}) profiles at a horizontal plane 14 cm from the wafer plane: (a) uniform power deposition without a focus ring, (b) uniform power deposition with a focus ring, (c) nonuniform power deposition without a focus ring, and (d) nonuniform power deposition with a focus ring.

planes near the upper wall, however, surface recombination losses come into play and destroy the Cl atoms. Thus a “hole” in the Cl atom concentration forms. At axial planes away from the top, this hole can fill in and the radial profile of Cl atoms can actually have a maximum at the reactor’s center. Near the cylindrical wall, the Cl atom density drops due to surface recombination losses. In the nonuniform power deposition cases the Cl density shows a peak at the azimuth of highest power absorption. The effect of the gas inlets is also evident in the Cl profiles, with local density

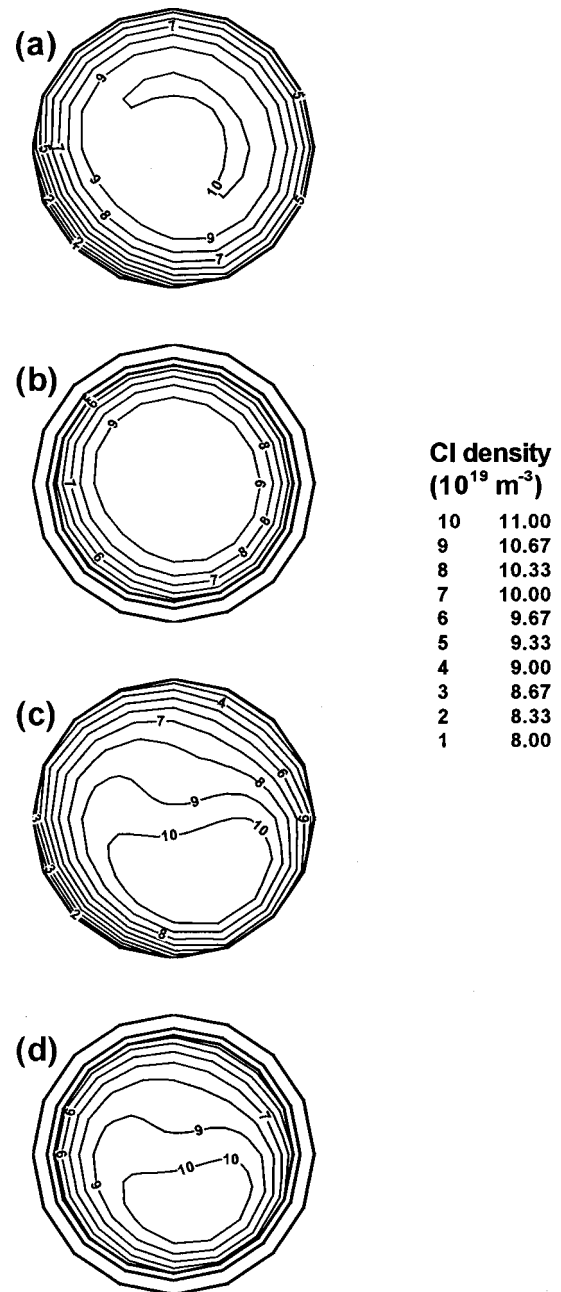


FIG. 6. Cl density (m^{-3}) profiles at the wafer plane: (a) uniform power deposition without a focus ring, (b) uniform power deposition with a focus ring, (c) nonuniform power deposition without a focus ring, and (d) nonuniform power deposition with a focus ring. For cases (b) and (d), the profiles are plotted over the region within the focus ring only.

perturbations. The presence of the pumping port at the reactor floor has only a small effect on the Cl density in the upper axial planes of the reactor.

The Cl^+ density profiles (Fig. 5) are qualitatively similar to the power deposition profiles, with the gradient of the Cl^+ distribution being steeper than that of Cl. Since ionization has a higher threshold energy compared to dissociation, the production of Cl^+ more closely mirrors the power deposition profile. It is also notable that the effect of inlet ports is not visible in the Cl^+ density profiles. The Cl^+ profile is a bit more uniform azimuthally when a focus ring is used, again mirroring the power deposition behavior. Slight azimuthal

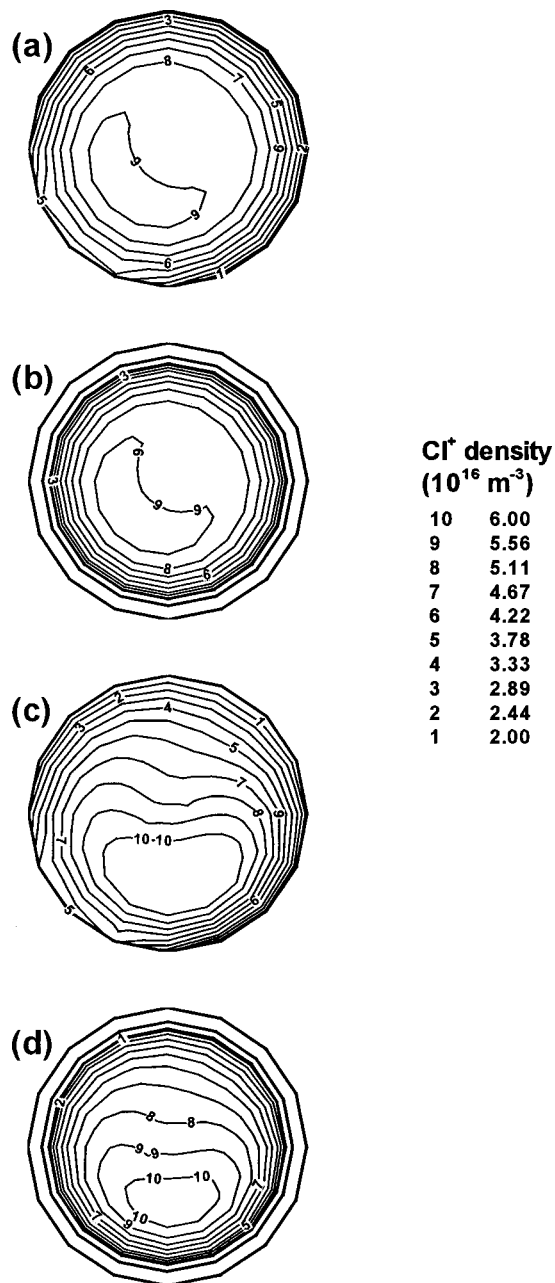


FIG. 7. Cl⁺ density (m⁻³) profiles at the wafer plane: (a) uniform power deposition without a focus ring, (b) uniform power deposition with a focus ring, (c) nonuniform power deposition without a focus ring, and (d) nonuniform power deposition with a focus ring. For cases (b) and (d), the profiles are plotted over the region within the focus ring only.

nonuniformities in the Cl⁺ profiles for the uniform power deposition cases [(a) and (b)], are thought to be caused mainly by the pumping port. The absence of the cylindrical wall at the pumping port results in longer diffusion length of ions in that region, and a locally higher ion density. The effect is felt even at the axial planes higher up in the reactor.

As species diffuse toward lower axial planes, the effect of inlet ports should become weaker, while the effect of pumping should become stronger for the reactor design considered [Fig. 2(a)]. Figure 6 shows the distribution of the Cl density on the wafer plane. The disturbance generated by the inlet ports near the top part of the reactor (Fig. 4) has com-

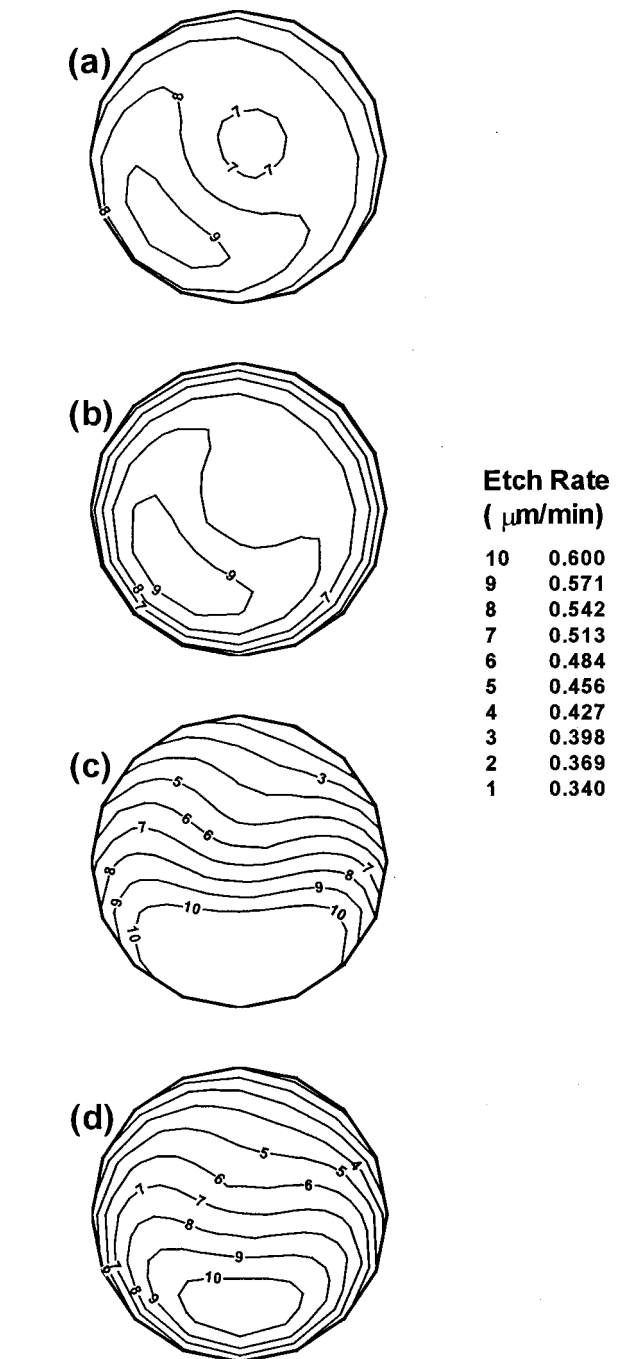


FIG. 8. Etch rate (μm/min) distribution across the Si wafer: (a) uniform power deposition without a focus ring, (b) uniform power deposition with a focus ring, (c) nonuniform power deposition without a focus ring, and (d) nonuniform power deposition with a focus ring.

pletely disappeared. The Cl density is lower at the azimuth of the pumping port [cases (a) and (c)] due to the depletion (removal) of neutral particles in that region. This is not evident in cases (b) and (d) due to shielding of the pumping port by the focus ring. The effect of nonuniform power deposition is clearly seen in cases (c) and (d). The distribution of the Cl⁺ ion density at the wafer level is also disturbed by the pumping port (Fig. 7). However, the dominant effect for cases (c) and (d) is the nonuniform power deposition that persists down to the wafer level. The ion density is a bit

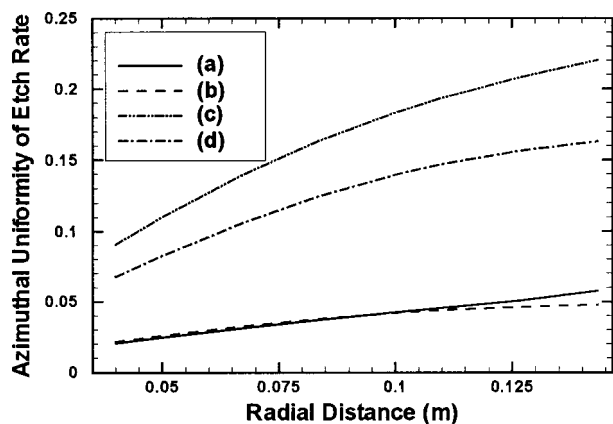


FIG. 9. Azimuthal uniformity index of the etch rate: (a) uniform power deposition without a focus ring, (b) uniform power deposition with a focus ring, (c) nonuniform power deposition without a focus ring, and (d) nonuniform power deposition with a focus ring.

lower in the presence of the focus ring due to recombination losses on the surface of the ring.

It was assumed that the etch reaction is ion induced and that the Cl^+ ion has a four times higher yield than the Cl_2^+ ion. Therefore, it is not surprising that the distribution of the etch rate along the wafer (Fig. 8) is similar to that of the Cl^+ ion density.

To quantify the effect of reactor design on azimuthal asymmetries, an *azimuthal* uniformity index (aziUI) was defined based on

$$f_{\text{avg}} = \sum_i^n f_i / n,$$

$$\text{aziUI} = \sqrt{\sum_i^n (f_i / f_{\text{avg}} - 1)^2 / (n - 1)},$$

where f_i is a quantity of interest at node i and n is the total number of nodal points at a given radial distance from the wafer's center. The azimuthal uniformity index is evaluated only over the wafer area. The lower the value of aziUI, the better the azimuthal uniformity.

The azimuthal uniformity index as a function of the radial distance is shown in Fig. 9 for the etch rate and in Fig. 10 for the Cl atom density. The focus ring improves the azimuthal uniformity significantly, especially in the nonuniform power deposition cases. In the uniform power deposition cases, a focus ring improves the azimuthal uniformity at larger radial distances, albeit only slightly.

IV. CONCLUSIONS

Two-dimensional simulations of plasma reactors are useful for predicting radial nonuniformities of plasma processes. However, a three-dimensional simulation is necessary for capturing nonazimuthal asymmetries introduced by inlet and pumping ports and azimuthally nonuniform inductive power deposition. This becomes more important as the wafer size keeps increasing to 300 mm and beyond in diameter. A three-dimensional finite element fluid model and a corresponding simulation tool, MPRES-3D, were developed for studying

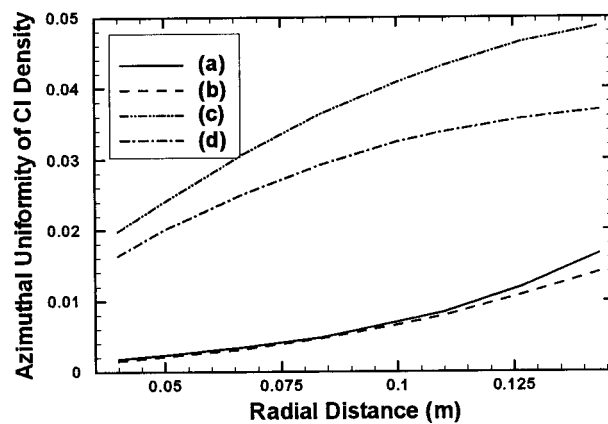


FIG. 10. Azimuthal uniformity index of the Cl atom density: (a) uniform power deposition without a focus ring, (b) uniform power deposition with a focus ring, (c) nonuniform power deposition without a focus ring, and (d) nonuniform power deposition with a focus ring.

azimuthal asymmetries and their effect on etch uniformity in inductively coupled plasma reactors. For silicon etching with chlorine in an ICP with a stovetop (planar) coil, four different cases were examined: (a) azimuthally uniform power deposition without a focus ring, (b) azimuthally uniform power deposition with a focus ring, (c) nonuniform power deposition without a focus ring, and (d) nonuniform power deposition with a focus ring. When the etching was ion driven, the power deposition profile was the most important for etch uniformity. This is because azimuthal nonuniformities in the ion production rate can persist even down to the wafer level. For uniform power deposition, the effect of asymmetric pumping became more important. A focus ring could significantly reduce azimuthal nonuniformities, especially in the nonuniform power deposition cases. Gas inlets pointing parallel to the wafer plane introduced only local disturbances in the species profiles, and had no noticeable effect on the etch rate.

ACKNOWLEDGMENTS

The authors are grateful to the National Science Foundation (CTS-9713262 and CTS-0072854) and the NSF-supported MRSEC at the University of Houston (DMR-9632667) for financial support of this work.

¹M. A. Lieberman and A. J. Lichtenberg, *Principles of Plasma Discharges and Materials Processing* (Wiley, New York, 1994).

²D. P. Lymberopoulos and D. J. Economou, *IEEE Trans. Plasma Sci.* **23**, 573 (1995).

³J. D. Bukowski and D. B. Graves, *J. Appl. Phys.* **80**, 2614 (1996).

⁴P. L. G. Ventzek, T. J. Sommerer, R. J. Hoekstra, and M. J. Kushner, *J. Vac. Sci. Technol. B* **12**, 461 (1994).

⁵T. Kimura, A. J. Lichtenberg, and M. A. Lieberman, *Plasma Sources Sci. Technol.* **10**, 430 (2001).

⁶D. Bose, T. R. Govindan, and M. Meyyappan, *J. Electrochem. Soc.* **146**, 2705 (1999).

⁷M. J. Kushner, W. Z. Collison, and M. J. Grapperhaus, *J. Appl. Phys.* **80**, 1337 (1996).

⁸M. J. Kushner, *J. Appl. Phys.* **82**, 5312 (1997).

⁹D. J. Economou, T. L. Panagopoulos, and M. Meyyappan, *Micro* **16**, 101 (1998).

¹⁰R. Wise, D. Lymberopoulos, and D. J. Economou, *Appl. Phys. Lett.* **68**, 2499 (1996); R. S. Wise, D. P. Lymberopoulos, and D. J. Economou, in *Proceedings of the 11th Plasma Processing Symposium*, edited by G. S.

- Mathad, M. Meyyappan, and D. W. Hess (The Electrochemical Society, Pennington, NJ, 1996), Vol. PV-96-12, p. 11.
- ¹¹D. J. Economou, J. Feldsien, and R. S. Wise, in *Electron Kinetics and Applications of Glow Discharges*, edited by U. Kortshagen and L. D. Tsendin, NATO Advanced Research Workshop (Plenum, New York, 1998).
- ¹²E. F. Jaeger, L. A. Berry, J. S. Tolliver, and D. B. Batchelor, *Phys. Plasmas* **2**, 2597 (1995).
- ¹³V. Midha and D. J. Economou, *J. Electrochem. Soc.* **144**, 4062 (1997).
- ¹⁴T. Panagopoulos and D. J. Economou, *J. Appl. Phys.* **85**, 3435 (1999).
- ¹⁵P. A. Miller and M. E. Riley, *J. Appl. Phys.* **82**, 3689 (1997).
- ¹⁶S. J. Choi and R. Veerasingham, *J. Vac. Sci. Technol. A* **16**, 1873 (1998).
- ¹⁷V. I. Kolobov and D. J. Economou, *Plasma Sources Sci. Technol.* **6**, R1 (1997).
- ¹⁸V. Vahedi, M. A. Lieberman, G. DiPeso, T. D. Rognlien, and D. Hewett, *J. Appl. Phys.* **78**, 1446 (1995).
- ¹⁹P. J. Chantry, *J. Appl. Phys.* **62**, 1141 (1987).
- ²⁰J. P. Chang, J. C. Arnold, G. C. H. Zau, H.-S. Shin, and H. H. Sawin, *J. Vac. Sci. Technol. A* **15**, 1853 (1997).